Feasibility Study of Planar-Array Electromagnetic Inductance Tomography (EMT)

S Ramli[1], A J Peyton[2]

[1] Engineering Unit, Malaysian Institute for Nuclear Technology Research (MINT), 43000 Kajang, Malaysia, shaharum@mint.gov.my
[2] Engineering Department, Lancaster University, Lancaster LA1 4YR, UK, a.peyton@lancaster.ac.uk

Abstract *– Many previously reported studies using electrical tomography have involved circular or near circular sensor arrays. In many situations, the object space has circular geometry and access is freely available around the complete periphery for installation of individual sensor elements. However there are some applications where access is restricted and non-invasive measurements can only be taken from one surface.*

This paper describes a study using EMT techniques to obtain cross-sectional images perpendicular to a measurement plane. The motivation for this research was to assess the feasibility of using a planar EMT sensor to inspect the distribution of electrically conductive bars using measurements from only one surface.

The study makes extensive use of 2D parametric finite element simulation in order to assess the feasibility of this approach. An iterative SIRT type image reconstruction algorithm has been employed and images from a variety of object geometries have been obtained which illustrate the potential and limitations of this method.

Keywords : Sensors, Tomography, Inductance, Planar

1. INTRODUCTION

Many previously reported studies using electrical tomography have involved circular or near circular sensor arrays. In many situations, the object space has circular geometry and access is freely available around the complete periphery for installation of individual sensor elements. However there are many situations where access is restricted and non-invasive measurements can only be taken from one surface.

This paper describes a study using EMT techniques [1,2] to obtain cross-sectional images perpendicular to a measurement plane. The motivation for this research was to assess the feasibility of using a planar EMT sensor to inspect the distribution of electrically conductive bars using measurements from only one surface.

The research described here has particular reference to the non-destructive testing of the integrity of steel reinforcing elements such as re-bars in concrete structures. This application is of importance because the steel components often impart much of the strength of the structure, especially in regions of high-applied tensile stress. A major potential problem with the structural integrity of steel reinforced concrete lies in the vulnerability of the steel elements to corrosion [3]. The traditional inspection method is to use core sampling, but in recent years alternative non-destructive techniques based on a variety of sensing principles have been researched. Inspection using AC magnetic fields in particular offers several practical advantages such as portability and intrinsic safety. To date promising results have been obtained by the method of scanning the surface and using image enhancement techniques [4,5]

The paper presents the results of an investigation into a novel form of planar-array electromagnetic tomography (EMT). Here, the excitation coils and detectors are arranged in a single plane, i.e. on the same side of the object space. Different ‘projections’ are obtained by energising the coils sequentially without the need for moving parts. At this stage, the aim of the study is just to demonstrate the potential and optimising the image reconstruction is not of prime concern.

2. SENSOR MODEL AND SIMULATION

A sensor design was studied by simulation using the 2D parametric modelling package Maxwell

produced by the Ansoft Corporation. The design of the sensor array was based on the experience gained from the investigation of circular geometries [6,7] and borrowed features from these, which were considered to be advantageous.

The following diagram shows the model of the sensor array. This consists of an aluminium backing plate, a bonded ferrite composite ferrite / epoxy soft magnetic screen, 16 ferrite poles and 16 excitation / detection coils. The backing plate and the composite screen help to ensure that the sensor is preferentially sensitive to the lower half plane (positive *y*). The soft magnetic screen is modelled with μ_R = 20, and consequently provides a low reluctance return path for the magnetic flux and hence minimises flux leakage into the upper half plane. Each excitation / detection coil is mounted on its own solid ferrite pole which acts as a flux concentrator.

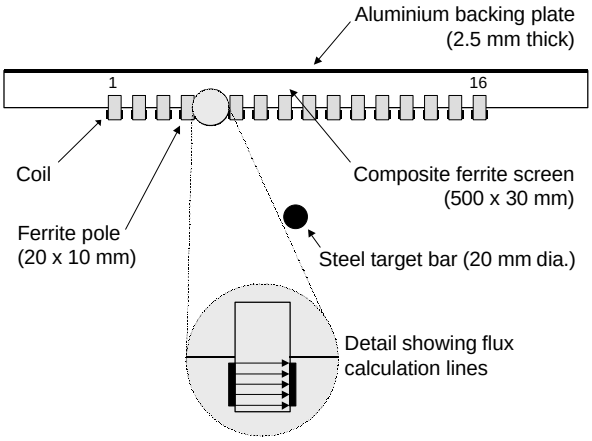

Figure 1: Cross-sectional view of the model of the sensor array

Figure 2 shows a plot of magnetic equi-potentials (flux plot) from one particular simulation with coil 8 energised by a 100 kHz alternating current. This diagram illustrates the low reluctance path offered by the composite screen, the flux concentration action of the ferrite poles and the effect of 20 mm diameter steel rebar positioned at (*x* = 0, *y*=4 cm).

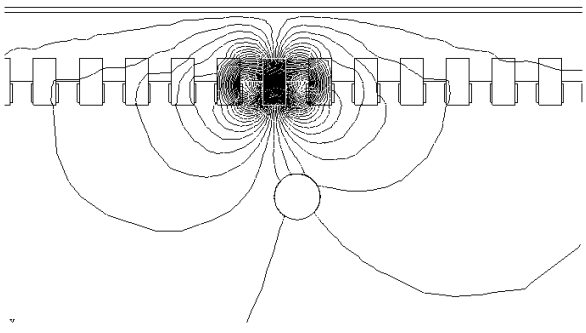

Figure 2: Plot of magnetic flux for coil 8 energised with a rebar positioned in the centre and 5 cm deep

The data required for image reconstruction was obtained by energised each of the 16 coils in turn with a 100 kHz, 1 A-turn, alternating current. While each coil was energised, the individual values of the flux linking all of the 16 coils were computed. The value for each coil was calculated as the average of the flux passing through 5 equally spaced lines, as shown in Figure 1 earlier. A total of 16 x 16 = 256 complex values were obtained for each frame. In this study only the real components of the data was used in order to limit the scope of the investigation.

3. SENSITIVITY MAPS

For this sensor, a sensitivity map was defined as the response of a particular detector element to the (*x, y*) position of a small perturbation, when a specific excitation coil was energised. In effect, the sensitivity map describes the response of the system to every pixel, for the selected excitation and detection coil pair. The perturbation was modelled as a 20 mm diameter steel bar with an electrical conductivity, s = 1x10^6 S/m and a relative permeability, m_R = 1000. A circular steel bar was chosen because of the interest in rebar studies and the diameter of 20 mm enabled the simulator to calculate sufficient signal changes excessive computational demands. For each sensitivity map, the bar was swept over the object space, which was defined as the area 20 cm deep and 35 cm across as shown in Figure 3. Finally, the signal changes due to the perturbation were obtained by subtracting the corresponding empty space values from the values with the bar present.

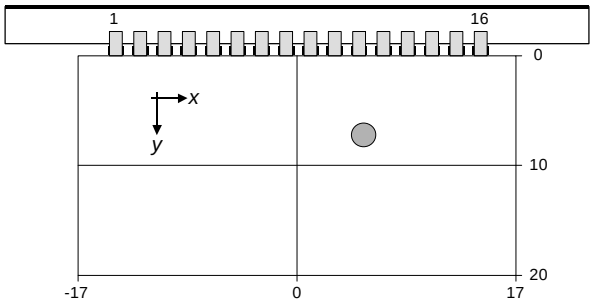

Figure 3: Definition of the object space (in cm)

The response of the full sensor array was described with a set of 256 (16 x 16) individual sensitivity maps, which corresponded to all the possible combinations of excitation and detection coils. Naturally, symmetry could be used to reduce the required calculations by one-half, as the response of the left-hand side of the sensor array is the same as the right. Despite this however, considerable computation was still required, which consisted of a total of 94,080 (21 x 35 x 16 x 8) individual FE simulations, to produce the data for the full set of sensitivity maps. Finally the data was extracted from the Maxwell files and manipulated into a suitable format for subsequent analysis using several programmes written in Visual Basic.

The FE simulator contained an automatic mesh generator and used an iterative procedure to obtain a solution. After each iteration, the simulator refined the mesh by adding more triangles until either a specified error was achieved or the number of passes reached the pre-set maximum. The most appropriate value for the target error was a compromise between accuracy and computational load and was decided by trial and error. Initially one map was computed to an error of less than 0.01%. Subsequently, the error was increased and the resulting maps were filtered to reduce noise. An energy error and a delta error 0.5 % were found to be sufficient for the purposes of this study.

Examples of three sensitivity maps are shown in Figure 4 for different combinations of excitation and detection coils.

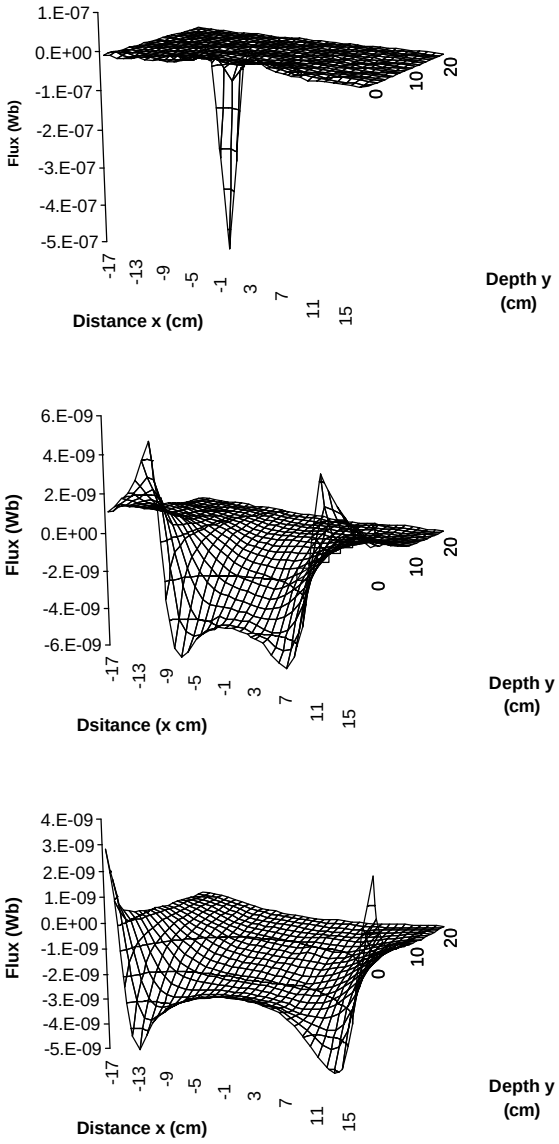

Figure 4: Different sensitivity maps for different excitation-detection coil separations
Top: Coil 8 excitation, coil 9 detection.
Middle: Coil 4 excitation, coil 13 detection.
Bottom: Coil 1 excitation, coil 16 detection.

The three plots show the general trends. First, as the detection and excitation elements are separated, the overall sensitivity reduces (notice the change in the Z-axis scale). Second, as the coils move apart (from top plot to bottom), the sensitive contours penetrate deeper into the object space. In simple terms, when the excitation / detection coils are close together, the system is relatively more sensitive to the surface layers. When the coils are further apart, the system becomes sensitive, in relative terms, to deeper features. It is this distinction of spatial sensitivity with coil position that this study attempts to exploit for tomographic imaging.

A final point to note is that the sensitivity maps display both positive and negative flux values. For example in the middle plot (coil 4 excitation, coil 13 detection), the flux is negative when the target bar is between the coils. This is because the bar acts as an electromagnetic screen and its induced eddy currents act to reduce the coupling. When the bar is more towards the periphery (e.g. $|x| > 10$ and $|y| < 10$), more flux couples to the detection coils because this presents a lower reluctance path. Although the total flux generated by the excitation coil is reduced.

4. IMAGE RECONSTRUCTION

The algorithms studied for this paper are based on the Simultaneous Increment Reconstruction Technique approach (SIRT) and the sensitivity maps described in the previous section are an essential part of this technique.

The data from a complete set of sensitivity maps were organised into a single 2 dimensional matrix, with 256 rows and 735 columns, which describes the response of the system to every pixel, for every detection coil, with each excitation coil energised in turn. The 256 rows correspond to the measurements from the 16 excitation and 16 detection coils, and the 735 columns correspond to the 21 pixel deep (0 to 20 cm inclusive) and 35 pixel wide (-17 to 17 cm inclusive) object space. This matrix characterises the complete system response and has been termed the projection matrix, **A**. If the object space is assumed to present a linear response, interactions between objects are ignored, then a crude system model can be written as:

$$\boldsymbol{p} \approx \boldsymbol{A.f} \qquad (1)$$

Vector ***f*** contains the image pixel values arranged as a column and contains 735 elements, where this is the total number of pixels in the object space as mentioned earlier. The corresponding measurement values are arranged in a vector ***p***.

Note ***p*** contains the changes in the measurement values caused by the object material. The background or empty space values must first be subtracted. Vector ***p*** contains 256 elements; this is the total number of measurements as described above. The actual number of independent values is 136 (i.e. $\frac{1}{2}N(N+1)$ where *N* is the number of poles) due to the reciprocity of mutual inductance. The full 256 element measurement set was not reduced to remove this redundancy because it was hoped that the extra measurements would help to increase signal-to-noise ratio, although this assumption has yet to be tested.

The SIRT-type algorithm used involves an iterative process to solve equation (1) for ***f*** when ***A*** and ***p*** are known. The basic iterative procedure can be described as follows. First, an initial guess, $\boldsymbol{f}^{(0)}$ is made for ***f***. Then, in each iterative step, the current estimation of the image is used to compute $\boldsymbol{f}^{(k+1)}$. The vector modification to $\boldsymbol{f}^{(k)}$ is made proportional to the error vector defined by the difference between the components of the measurement vector and the estimated measurement vector $\boldsymbol{p}_{est}^{(k)}$ from $\boldsymbol{p}_{est}^{(k)} = \boldsymbol{A}.\boldsymbol{f}^{(k)}$. The pixel values were also constrained to be positive. The iterative step is

$$\boldsymbol{f}^{(k+1)} = \boldsymbol{f}^{(k)} + l\,\boldsymbol{S}.(\boldsymbol{p}^{(k)} - \boldsymbol{A}.\boldsymbol{f}^{(k)}) \text{ or } 0 \qquad (2)$$

The value l is a relaxation constant, which was chosen to optimise convergence. Matrix ***S*** contains sensitivity coefficients relating the effects of particular measurement to pixel values, as described shortly. Convergence to a reasonable limit is only assured in the linear case. In general, the speed of convergence depends on many factors such as the initial estimation, a parameter controlling the convergence speed, and the order on which the various system equations (projection matrix lines) are solved. The algorithm must be previously tuned using test images in order to expect reasonable results in the actual application. The operation of the algorithm is summarised in figure 5.

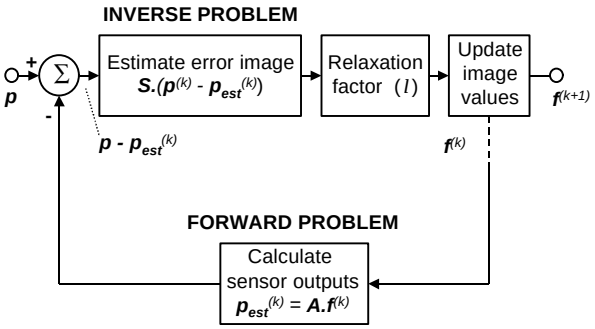

Figure 5: Operation of the reconstruction algorithm

The matrix ***S*** can be determined from the physical model of the system. Ideally ***S*** would simply be $\boldsymbol{A}^{-1}$, however normally ***A*** cannot be inverted, so an approximate process of transposing and normalising each line was used to produce $\boldsymbol{S}_1$, as follows:

$$s_i = \frac{a_i^T}{\left\| a_i^T \right\|^2} \qquad (3)$$

An alternative $\boldsymbol{S}_2$ to the simple transpose and normalisation approach was also tested. This involved conditioning the matrix as follows.

$$\boldsymbol{S}_2 = (1+h)\left[\boldsymbol{S}_1.\boldsymbol{A} + h\boldsymbol{I}\right]^{-1}.\boldsymbol{S}_1 \qquad [4]$$

The value of η = 1 was determined by trial and error. If η is too small then the matrix cannot be inverted.

5. RESULTS

Measurements for a number of object distributions were simulated. The value of the relaxation constant needed to be relatively small (typically λ = 0.00 1 to 0.001) in order to ensure convergence. This value is considerably smaller than that used on circular EMT arrays and meant that a large number of iterations were needed (typically several thousand) until a final image had stabilised. The mean and RMS measurement errors ($\boldsymbol{p}$ - $\boldsymbol{p}_{est}^{(K)}$) were monitored in order to determine when to terminate the iterative process. Figure 6 shows a typical plot with l = 0.001, using $\boldsymbol{S}_1$ to perform the inverse solution.

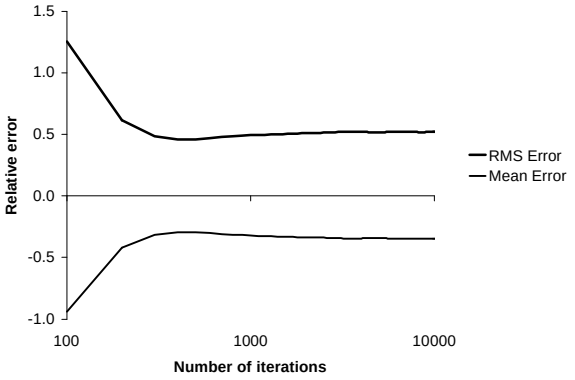

Figure 6: Plot showing the convergence of the reconstruction algorithm

The following sub-sections contain image plots from various tests performed on the algorithms. These include single bars inside and outside the object space, single bars with different diameters, two bars separated horizontally and vertically in order to assess spatial resolution, 6 bar arrangements and a selection of steel plates.

5.1. Single bar inside the object space

Figure 7 shows a set of image plots of a single bar (diameter 2 cm) placed at either (*x*=0, *y*=5 cm), or (*x*=0, *y* =15 cm). Plots (a) and (c) use $\boldsymbol{S}_1$ for the inverse matrix, whereas plots (b) and (d) use $\boldsymbol{S}_2$.

The ideal plot would be a single pixel with a value of 1 at the bar position with all other pixels equal to zero. In general, $\boldsymbol{S}_2$ produced slightly sharper images of the bar than $\boldsymbol{S}_1$, however the baseline noise was often much higher. Consequently, $\boldsymbol{S}_1$ is used in preference in all the following sub-sections.

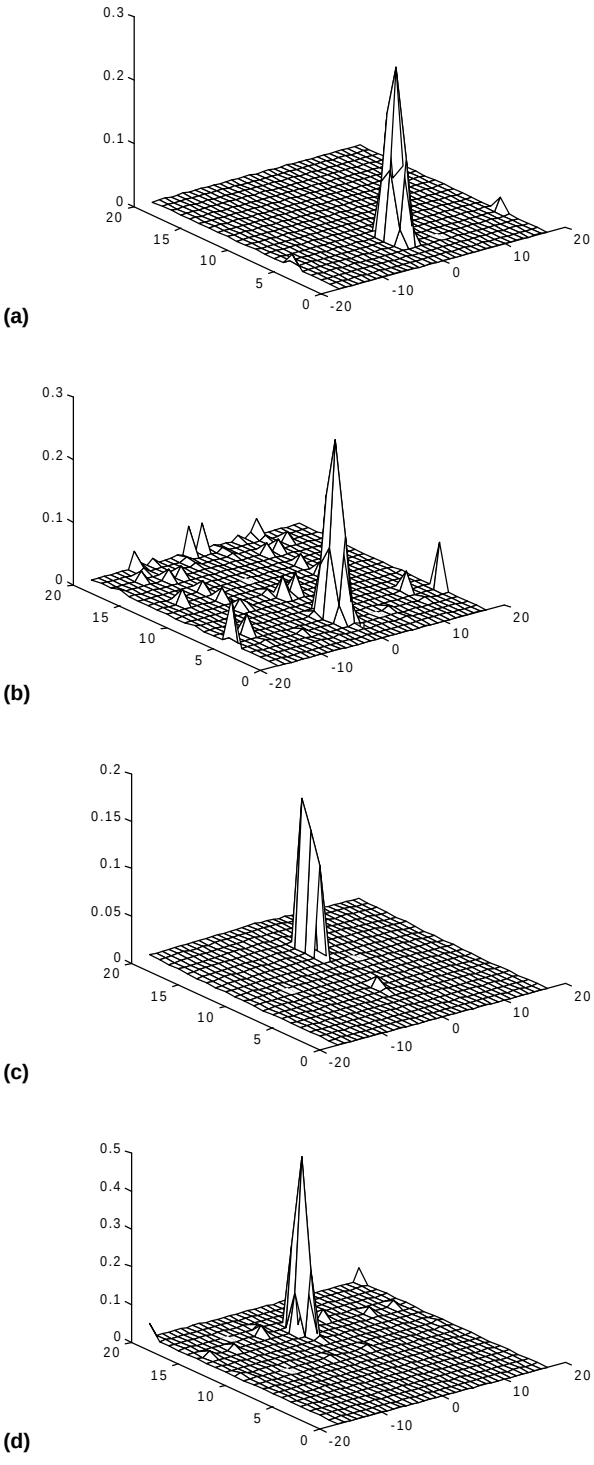

Figure 7: Image plot of single steel bars (2 cm diameter)
(a) Position (0, 5), λ = 0.001, 5000 iterations, with S_1
(b) Position (0, 5), λ = 0.01, 5000 iterations, with S_2 (μ = 1)
(c) Position (0, 15), λ = 0.001, 5000 iterations, with S_1
(d) Position (0, 15), λ = 0.01, 5000 iterations, with S_2 (μ = 1)
Note *x*, *y* scales are in cm, *z* scale is in relative units.

5.2. Single bar outside the object space

The effect of a single bar positioned outside the object space was to produce spurious values on the boundary. This effect is shown in Figure 8 for a bar positioned just outside the target area and at a depth of 5 cm. Ideally, the algorithm should return all zero values for the pixels. This diagram illustrates the limitations of using a finite object space to determine the projection matrix.

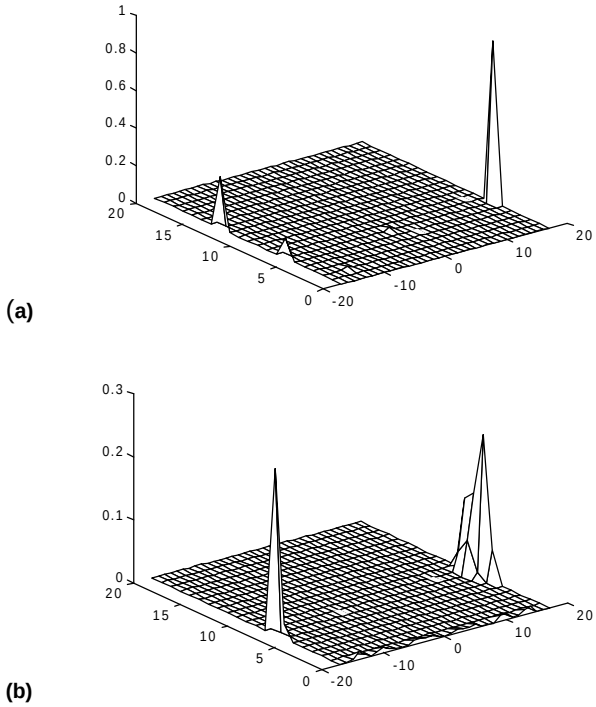

Figure 8: Image plot of single steel bars (2 cm diameter) outside the object space.
(a) Position (18, 5), λ = 0.01, 5000 iterations
(b) Position (19, 5), λ = 0.01, 5000 iterations
Note *x*, *y* scales are in cm, *z* scale is in relative units.

5.3. Effect of bar diameter

Figure 9 shows the effects of the diameter of the rod on the image plots and gives an indication of the difficulties in determining the diameter using this algorithm. For a small diameter of 0.5 cm (Figure 9(a)) the image is very noisy, as the measurement values are small compared to the simulator errors, note the small *z* scale. As the bar diameter gets bigger (figure 9(b)), then the bar comes more clearly into view and the pixel values get larger. For a very large diameter bar, i.e. 6 cm diameter, the image plot is a very poor representation. In effect the algorithm attempts to represent the larger bar with two smaller objects at the front and rear. These artefacts are possibly caused by the skin effect due to the field changes caused by surface eddy currents in these regions.

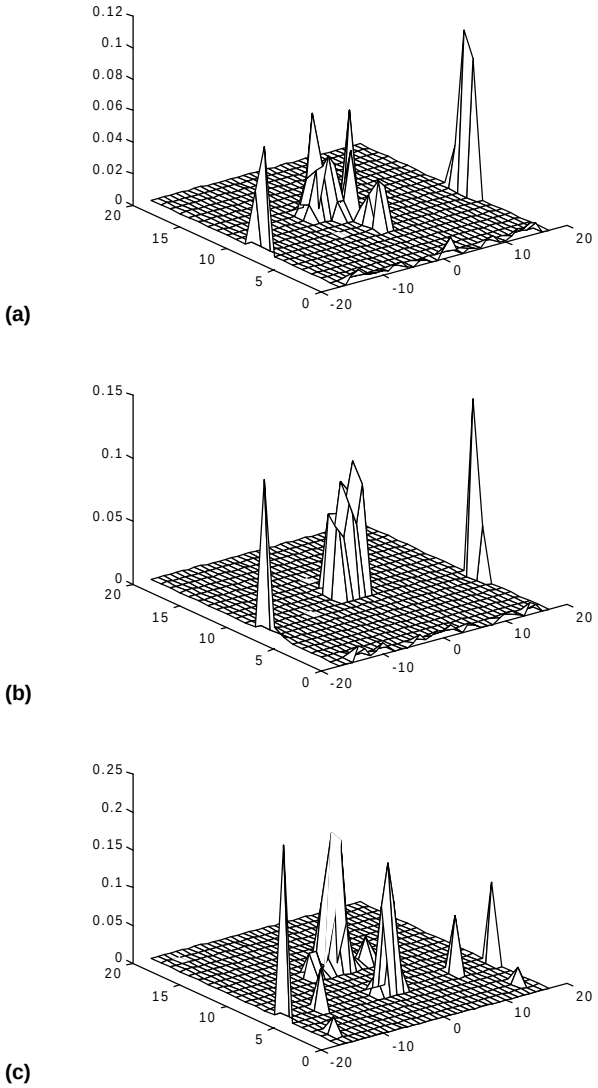

Figure 9: Image plot of a single steel bars with different diameters placed at *x*=10, *y*=10 cm.
(a) Diameter 0.5 cm, λ = 0.001, 5000 iterations
(b) Diameter 1.0 cm, λ = 0.001, 5000 iterations
(c) Diameter 6.0 cm, λ = 0.001, 5000 iterations
Note *x*, *y* scales are in cm, *z* scale is in relative units.

5.4. Assessment of spatial resolution

A limited assessment of spatial resolution was attempted by simulating the effects of two 20 mm diameter, steel bars, with varying degrees of separation. The ability of the algorithm to distinguish the horizontal features was different to the vertical case, as shown in the following two sets of diagrams.

Figure 10 shows image plots obtained from two bars positioned horizontally to each other, 5 cm deep, and separated with a gap of 0, 2 cm and 14 cm respectively. As the diagram shows, when the bars are close together they tend to merge into each other. For example in Figure 10(a), the plot displays only one central peak for both bars. The peak, however, this is larger than that of a single 20 mm diameter bar shown earlier in Figure 7(a). This effect can also be seen in Figure 10(b) with a single peak, which is horizontally elongated. It is not until the gap is several cm (i.e. much greater than one diameter) that the bars can readily be distinguished from each other.

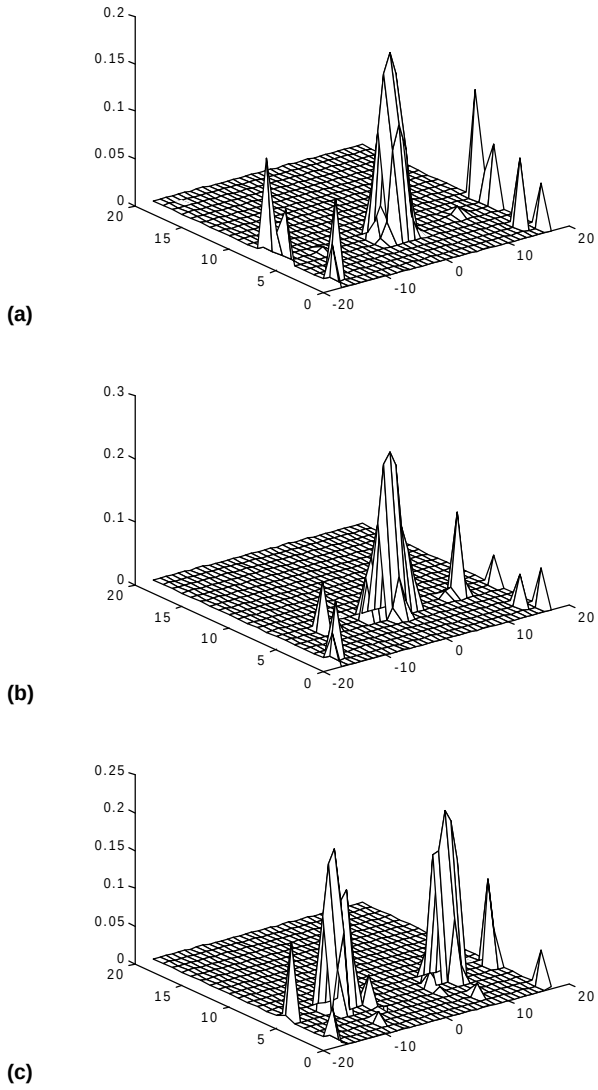

Figure 10: Image plot of two steel bars, 20 mm diameter and 5 cm deep, with different horizontal separations.
(a) Separation 0 cm, λ = 0.001, 500 iterations
(b) Separation 2 cm, λ = 0.001, 5000 iterations
(c) Separation 14 cm, λ = 0.001, 5000 iterations
Note *x*, *y* scales are in cm, *z* scale is in relative units.

Figure 11 shows image plots from two 20 mm diameter steel bars positioned centrally, but separated vertically with gaps of 0, 2, 6, and 8 cm. When the bars are touching, Figure 11(a), the plot shows only a single peak, however this is bigger than that for a single bar alone. As the bars move apart, Figure 11(b), a single, vertically elongated peak can be seen. Again, it is not until the gap is several cm (i.e. at least one diameter) that the bars can readily be distinguished from each other, Figure 11(c). However, if the a gap is too large, then the bar nearest to the sensor tends to screen the effects

of the deeper bar, which appears smaller and incorrectly positioned in Figure 11(d).

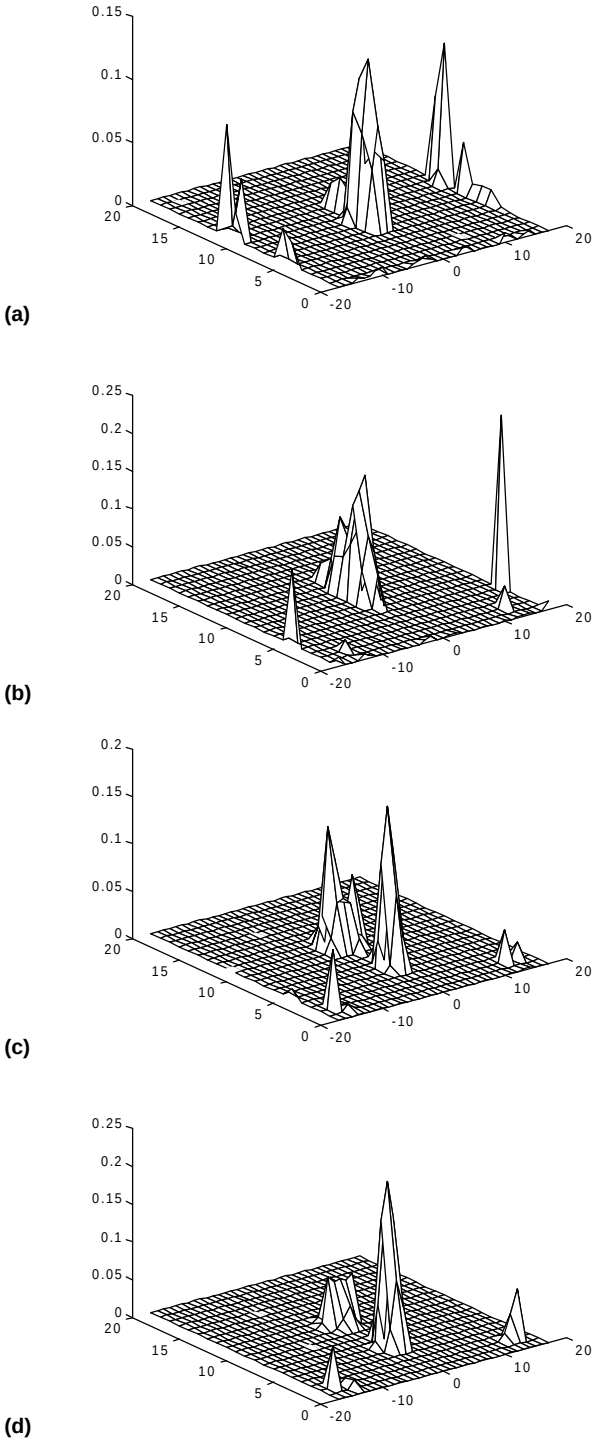

Figure 11: Image plot of two steel bars, 20 mm diameter centrally placed, with different vertical separations.
(a) Gap 0 cm (*y* = 9 & 11 cm), λ = 0.001, 500 iterations
(b) Gap 2 cm (*y* = 8 & 12 cm, λ = 0.001, 5000 iterations
(c) Gap 6 cm (*y* = 6 & 14 cm, λ = 0.001, 5000 iterations
(d) Gap 8 cm (*y* = 5 & 15 cm, λ = 0.001, 5000 iterations
Note *x*, *y* scales are in cm, *z* scale is in relative units.

5.5. More examples

Figure 12 shows an image plot obtained for six, 20 mm, steel bars placed in a rectangular pattern (two rows of three). The algorithm has been left to iterate 4 times longer than previously. The three bars in the upper row are clearly visible in the plot however; the deeper row of bars is scarcely detected, apart from a small artefact in the position of the lower central bar. The spurious boundary effects are not shown for clarity.

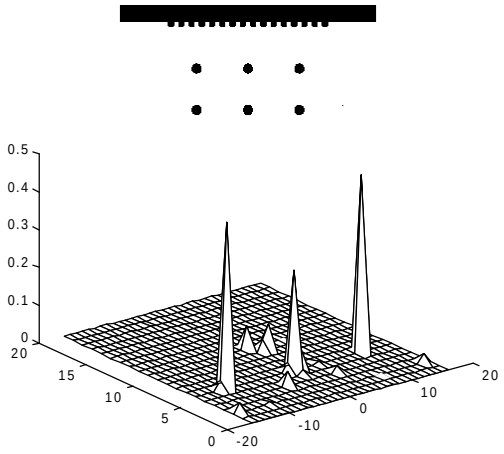

Figure 12: Image plot of six steel bars, 20 mm diameter, set out in 2 rows of 3. λ = 0.001, 20,000 iterations.
Positions, *y*=5, *x*= -10, 0, 10 cm
Positions, *y*=10, *x*= -10, 0, 10 cm
Note *x*, *y* scales are in cm, *z* scale is in relative units.

Figure 13(a) shows a test arrangements containing a steel plate, 10 mm thick. In one test, the plate has a notch 5 mm square inserted. Figure 13(b) shows the resulting image, which has features at the correct depth, but the plate is not very well represented. The notch has virtually no effect and in fact the same image is obtained for both plates. Figure 13(c) shows an image plot when the simulated measurement data from the two plates is first subtracted before being reconstructed. The position of the notch is now clearly visible, indicating the potential of this approach for identifying erroneous features in simple objects. Again, spurious boundary effects are not shown for clarity.

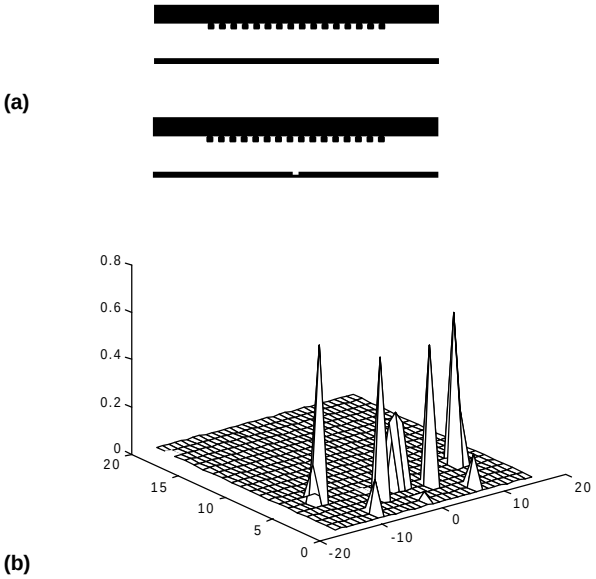

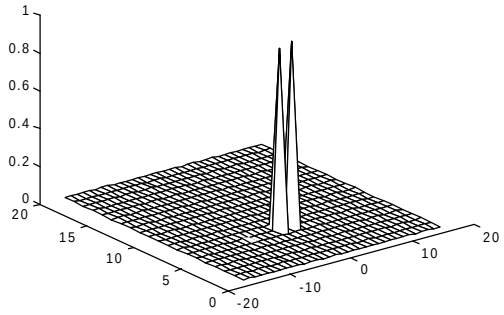

(c)

Figure 13: Image plot of a steel plate 10 mm thick with a 5mm square notch. λ = 0.01, 5,000 iterations.
(a) Test arrangement
(b) Image plot of both plates
(c) Image plot of the difference
Note *x*, *y* scales are in cm, *z* scale is in relative units.

6. FUTURE WORK AND CONCLUSIONS

The results presented in this paper suggest that EMT could be successfully applied to applications where the object space is not completely enclosed, however the results are based on simulations and limited to the 2D case. Therefore a degree of caution is necessary, but the results do strongly suggest the need for further research. Possible areas for further study include:

- Test the algorithm with measured data. Past experience with circular EMT sensors has generally shown that measured data produces similar if not better results than simulated due to quantisation errors arising from the finite mesh size.
- Better implementations of the SIRT algorithm. At present, no attempt has been made to optimise the implementation of the algorithm. For example, imaginary data is ignored, the object space is artificially bounded, the perturbation is relative large and may not be the most appropriate type of material, and redundant data is contained in the projection matrix, ***A***. The imaginary signals may be important in practice for rebar imaging because the imaginary components are strongly related to the losses caused by the induced surface eddy currents in the rebars. It is also likely that induced surface currents will be affected by surface corrosion on the bars.
- Three-dimensional studies. The ability to vary parameters and perform numerous individual FE simulations is very useful tool in developing electrical tomography systems. It is likely that sophisticated parametric 3D simulators will soon be available, which would enable more realistic studies to be performed.
- Improved algorithms. The algorithm used in this feasibility study is not tailored to one particular application and in practice the projection matrix represents a crude forward model of the system. It may be expected that a more realistic forward model, possible FE based, taking into account the knowledge of the material and reasonable assumptions on their distributions may be present a promising way forward.

REFERENCES

[1] Z.Z. Yu, A.J. Peyton, L.A. Xu and M.S. Beck, "*Electromagnetic inductance tomography (EMT): sensor, electronics and image reconstruction for a system with a rotatable parallel excitation field*", IEE Proc. Sci. Meas. Technol., **145**(1), pp. 20-25, 1998.

[2] A.J. Peyton, Z.Z. Yu, G.M. Lyon, S. Al-Zeibak, J. Ferreira, J. Velez, F. Linhares, A.R. Borges, H.L. Xiong, N.H. Saunders and M.S. Beck, "*An overview of electromagnetic inductance tomography: description of three different systems*", Meas. Sci. Technol., **7**, pp. 261-271, 1996.

[3] K.F. Dunker and B.G. Rabbat, "Why America's bridges are crumbling", Sci. Am., **268**(3), pp. 18-24, March 1993.

[4] P A Gaydecki and F M Burdekin, "*An inductive scanning system for two-dimensional imaging of reinforcing components in concrete structures*", Meas. Sci. Technol., **5**, pp. 1272-80, 1994.

[5] Z.Z. Yu, P. Gaydecki, "*One-dimensional current imaging based on an analytical solution of magnetic field distribution: applications to non-destructive testing of reinforcing bars in concrete*", Meas. Sci. & Technol., **9**(9), pp. 1571-75, 1998.

[6] J. Ferreira, F. Linhares, J. Velez, J. E. de Oliveira, and A.R. Borges, "*Imaging of conductive and ferromagnetic materials using a magnetic induction technique*", 12th annual review of progress in Applied Computational Electromagnetics, pp. 367-374, Monterey Ca. USA, 1996.

[7] A J Peyton, M S Beck, A R Borges, J E de Oliveira, G M Lyon, Z Z Yu, M W Brown, J Ferrerra, "*Development of Electromagnetic Tomography (EMT) for Industrial Applications. Part 1: Sensor Design and Instrumentation*", 1st World Congress in Industrial Process Tomography, Buxton UK, 13-17 April 1999.

[8] F. Natterer, "The mathematics of computerised tomography", Wiley, Chichester, 1986.